NASA MEMO 1-22-59L

NASA

MEMORANDUM

LOW-SUBSONIC STATIC STABILITY AND DAMPING DERIVATIVES AT ANGLES OF ATTACK FROM 0° TO 90° FOR A MODEL WITH A LOW-ASPECT-RATIO UNSWEPT WING AND TWO DIFFERENT FUSELAGE FOREBODIES

By Peter C. Boisseau

Langley Research Center
Langley Field, Va.

NATIONAL AERONAUTICS AND SPACE ADMINISTRATION

WASHINGTON
March 1959

NATIONAL AERONAUTICS AND SPACE ADMINISTRATION

MEMORANDUM 1-22-59L

LOW-SUBSONIC STATIC STABILITY AND DAMPING DERIVATIVES AT ANGLES OF ATTACK FROM 0° TO 90° FOR A MODEL WITH A LOW-ASPECT-RATIO UNSWEPT WING AND TWO DIFFERENT FUSELAGE FOREBODIES

By Peter C. Boisseau

SUMMARY

An investigation has been made in the Langley free-flight tunnel at low-subsonic speed to determine the static stability, control effectiveness, and damping in roll and yaw of a model with a low-aspect-ratio unswept wing and two different fuselage forebodies at angles of attack from 0° to 90°. Results were obtained with a fuselage configuration having a long pointed nose and a shorter rounded nose.

Although the wing stalled at an angle of attack of about 12°, maximum lift did not occur until an angle of attack of about 40° or 50° was obtained. The static longitudinal stability of the model having a short rounded nose was greater than that of the model having a longer pointed nose over the entire angle-of-attack range. The pointed-nose model had large out-of-trim yawing moments above an angle of attack of about 40°. Shortening and rounding the nose of the model delayed these out-of-trim yawing moments to slightly higher angles of attack. Both models were directionally unstable above an angle of attack of about 20°, but both had positive effective dihedral over virtually the entire angle-of-attack range. At the higher angles of attack the pointed-nose model had generally better damping in roll than that of the rounded-nose model. Both models had very high damping in yaw at an angle of attack of about 50° or 60°.

INTRODUCTION

A general investigation is being conducted by the National Aeronautics and Space Administration to provide aerodynamic information on which preliminary studies of the stability and handling qualities of vertical-take-off-and-landing airplanes can be based. This investigation consists of static-force tests and oscillation tests to measure the

stability and control characteristics at angles of attack from 0° to 90° of existing models of unswept-, sweptback-, and delta-wing airplanes which are generally representative of possible vertical-take-off-and-landing airplane configurations. As part of this general investigation, an exploratory investigation with a model having a low-aspect-ratio unswept wing has been undertaken to establish the trends in the various stability parameters in the high-angle-of-attack range for configurations of this general type.

In the present investigation measurements were made of the static longitudinal and lateral stability, longitudinal and lateral control effectiveness, and lateral damping derivatives of a model at angles of attack from 0° to 90°. The model was tested with a fuselage having a long pointed nose and a shorter rounded nose because preliminary data indicated that the pointed nose caused large variations in the lateral-stability data above an angle of attack of 40°. The results include data for the complete model and for the model with both vertical and horizontal tails removed.

SYMBOLS

The longitudinal-stability data are referred to the stability system of axes, and the lateral-stability data are referred to the body system of axes. (See fig. 1.) The origin of the axes was located to correspond to a center-of-gravity location at the 10-percent station of the mean aerodynamic chord of the wing.

S	wing area, sq ft
$\bar{c}$	mean aerodynamic chord, ft
V	free-stream velocity, ft/sec
b	wing span, ft
q	dynamic pressure, lb/sq ft
β	angle of sideslip, deg
ψ	angle of yaw, deg
ϕ	angle of bank, deg
α	angle of attack, deg (In tests where the model is rolled or yawed about the body axis, the angle of attack varies with angle of bank or angle of yaw. The angles of attack specified in this report are the angles measured at zero bank and zero yaw.)

X,Y,Z longitudinal, lateral, and normal body axes, respectively

X_S,Z_S longitudinal and vertical stability axes, respectively

M_{Y_S} pitching moment, ft-lb

M_X rolling moment, ft-lb

M_Z yawing moment, ft-lb

F_D' drag force, lb

F_L lift force, lb

F_Y lateral force, lb

C_D' approximate drag coefficient, F_D'/qS

C_L lift coefficient, F_L/qS

C_Y lateral-force coefficient, F_Y/qS

C_m pitching-moment coefficient, $M_{Y_S}/qS\bar{c}$

C_n yawing-moment coefficient, M_Z/qSb

C_l rolling-moment coefficient, M_X/qSb

$$C_{n_\psi} = \frac{\partial C_n}{\partial \psi} \text{ per degree}$$

$$C_{Y_\beta} = \frac{\partial C_Y}{\partial \beta} \text{ per degree}$$

$$C_{l_\beta} = \frac{\partial C_l}{\partial \beta} \text{ per degree}$$

$$C_{n_\beta} = \frac{\partial C_n}{\partial \beta} \text{ per degree}$$

$C_{n_r} = \frac{\partial C_n}{\partial \frac{rb}{2V}}$ per radian

$C_{l_p} = \frac{\partial C_l}{\partial \frac{pb}{2V}}$ per radian

$C_{n_{\dot{\beta}}} = \frac{\partial C_n}{\partial \frac{\dot{\beta}b}{2V}}$ per radian

$C_{l_{\dot{\beta}}} = \frac{\partial C_l}{\partial \frac{\dot{\beta}b}{2V}}$ per radian

p rolling angular velocity, radian/sec

r yawing angular velocity, radian/sec

$\dot{\beta}$ rate of change of angle of sideslip, radian/sec

δ_t horizontal-tail deflection, deg

δ_a aileron deflection, deg

δ_r rudder deflection, deg

ω angular velocity, radian/sec

k reduced-frequency parameter, $\omega b/2V$

Subscripts:

L left

R right

APPARATUS AND MODEL

The static force tests and free-to-damp oscillation tests were conducted in the Langley free-flight tunnel which is a low-subsonic wind tunnel with a 12-foot octagonal test section. The model was mounted in the tunnel with a sting-type support system and an internally mounted three-component strain-gage balance. A complete description of the static and oscillation equipment used in these tests is given in reference 1. A sketch of the oscillation equipment is shown in figure 2. The static-force-test setup was similar to the damping-in-roll-test setup shown in figure 2(a), with the exception that the static-test setup had provisions for yawing the model.

The model had a thin unswept wing of low aspect ratio and an all-movable horizontal tail. A three-view drawing of the model is shown in figure 3, and geometric characteristics of the model are given in table I. Two different forebodies were used on the fuselage in this investigation: a long pointed nose and a shorter rounded nose.

TESTS

Force tests were made to determine the static longitudinal and lateral stability and control characteristics of the model at angles of attack from 0° to 90°. The free-to-damp oscillation tests were made by use of the method described in reference 1 to determine the damping-in-yaw and damping-in-roll parameters at angles of attack from 0° to 90° for the same configurations tested in the static conditions. The model was tested with a long pointed nose and a shorter rounded nose, and the results include data for the complete model and for the model with both vertical and horizontal tails removed. All static-stability and damping tests were made at a dynamic pressure of about 4.58 pounds per square foot which corresponds to a free-stream velocity of about 62.2 feet per second and a Reynolds number of about 0.31×10^6 based on the mean aerodynamic chord.

No attempt was made in this investigation to determine the effect of changes in amplitude or frequency of the oscillation on the lateral damping. The oscillation tests were made at a frequency of about 1.0 cycle per second which corresponds to a reduced-frequency parameter k of 0.11. The model was displaced in yaw or roll about 30° before being released and allowed to damp to an amplitude of 0°. Four oscillation records were usually obtained at each angle of attack - a tare test with wind off to measure the residual friction damping of the system and three tests with wind on. Because of the strong restoring spring used in the oscillating test setup, the periods of the oscillations with wind off and wind on

were almost identical. The envelopes of the oscillations plotted on semilogarithmic paper were fairly linear through the amplitude range investigated except for small amplitudes where the tunnel turbulence caused the data to be erratic. Because of the nonlinearity of the data at the small amplitudes, the logarithmic decrements or damping factors used to determine the damping derivatives in this investigation were obtained from the slopes of the envelope curves for amplitudes above approximately $\pm 2^\circ$ or $\pm 3^\circ$. The damping derivatives were calculated from the test data by means of the methods used in reference 1.

Inasmuch as the primary purpose of this investigation was to obtain an indication of the trends of the various stability derivatives, particularly at high angles of attack, for a configuration of this general type rather than to obtain accurate quantitative information on a specific configuration, no attempt was made to correct the data to account for such factors as support interference, tunnel blockage and jet-boundary effects, and aerodynamic damping of the oscillating rig. On the basis of some exploratory work in previous investigations, it is believed that such corrections would not be large enough to alter significantly the trends of the data. In order to provide quantitatively accurate data, these corrections would be required.

RESULTS AND DISCUSSION

Static Longitudinal Stability and Control Characteristics

The static longitudinal stability and control characteristics of the pointed- and rounded-nose-model configurations are presented in figures 4(a) and 4(b), respectively. The data show a break in the lift curve for both models at an angle of attack of about 12°, but the lift continues to increase up to an angle of attack of about 50° for the pointed-nose model and up to an angle of attack of about 40° for the rounded-nose model. The data of figure 4(a) show that the pointed-nose model is unstable at angles of attack from about 12° to 20° and from about 40° to 70°. These results are generally similar to those found in reference 2 for low Reynolds numbers. The data of reference 2 also show that increasing the Reynolds number above about 0.600×10^6 had a large stabilizing effect on the model at the higher angles of attack. The data of figure 4(b) show that the rounded-nose model was longitudinally stable over the angle-of-attack range except at angles of attack from about 12° to 20° for $\delta_t = 0^\circ$ and -5°. The data of figure 4 show that some horizontal-tail effectiveness was maintained for both models beyond the angle of attack for maximum lift.

Lateral Stability and Control Characteristics

The variation of the lateral-force, yawing-moment, and rolling-moment coefficients with ψ is shown in figures 5 and 6 for the two configurations tested. The data of figure 5 for the pointed-nose configuration show that there were large out-of-trim yawing moments above an angle of attack of about 40° for both the complete model and the model with all tails off. The data of figure 6 show that shortening and rounding the nose of the model delayed the large out-of-trim yawing moments to a slightly higher angle of attack and reduced their magnitude to some extent. These data show that out-of-trim rolling moments were obtained which were much smaller than the out-of-trim yawing moments at the higher angle-of-attack range for all the conditions tested.

A number of check tests at $\psi = 0°$ were made to study further the large out-of-trim yawing moments at the higher angles of attack. The data obtained in these tests are presented in figure 7. The shaded area shows the range of readings obtained at the higher angles of attack. The data of figure 7 show that shortening and rounding the nose eliminated the large consistent change in out-of-trim yawing moment between angles of attack of 30° and 35° and delayed the large scatter of measured yawing moments to a higher angle of attack. Based on the results of figure 7 it appears that the individual yawing moments of figures 5 and 6 should not be considered reliable above an angle of attack of 40° or 50°. It was observed during these tests that the rolling moments did not experience large fluctuations and, therefore, the rolling-moment data are considered to be fairly reliable up to an angle of attack of 90°.

The results of figure 7 indicate that shortening and rounding the nose of the fuselage delayed the unsymmetrical shedding of fuselage vortices to a higher angle of attack. The data of reference 3 show that the use of a ring on the nose delayed the out-of-trim yawing moments of a pointed-nose fuselage to a higher angle of attack, apparently because the ring produced a more symmetrical shedding of vortices from the nose. Other studies have shown that the use of longitudinal nose strakes can produce a similar improvement in the out-of-trim yawing moment of models with pointed-nose fuselages.

Static lateral stability derivatives.- The sideslip derivatives presented in figure 8 were obtained from the static-stability data of figures 5 and 6 for amplitudes of ψ of ±5° by using the relationships presented in reference 1. $\left(\text{For example, } C_{n_\beta} = -\frac{C_{n_\psi}}{\cos \alpha}.\right)$ The data are shown only up to angles of attack of 40° and 50° because the data of figures 5 and 6 are not considered reliable above these angles. Both configurations became directionally unstable above an angle of attack of about 20° primarily because of a loss in tail effectiveness. Both

models had positive effective dihedral $-C_{l_\beta}$ over virtually the entire angle-of-attack range.

Lateral control.- The rudder- and aileron-effectiveness data are presented in figure 9 for the rounded-nose model. The rudder effectiveness is not shown above an angle of attack of 50° because of the previously mentioned unreliability of the yawing-moment data at the higher angles of attack. For the same reason, the lateral-force and yawing-moment data are not shown above an angle of attack of 50° in the aileron-effectiveness plot (fig. 9(b)). Both the rudder and aileron effectiveness decreased with increasing angle of attack, but some effectiveness was maintained over the angle-of-attack range shown.

Lateral damping derivatives.- Values of the damping-in-roll derivative $C_{l_p} + C_{l_{\dot\beta}} \sin \alpha$ and the damping-in-yaw derivative $C_{n_r} - C_{n_{\dot\beta}} \cos \alpha$ measured relative to the body axis and plotted against angle of attack are presented in figures 10(a) and 10(b), respectively, for both models with the tails on and off. These data are not considered very reliable above an angle of attack of about 50° because of the previously discussed out-of-trim yawing moments in this angle-of-attack range. These high-angle-of-attack data are included, however, because it is felt that they provide a qualitative indication of the damping even though the quantitative values shown are not considered reliable.

For the pointed-nose model, positive damping in roll $-\left(C_{l_p} + C_{l_{\dot\beta}} \sin \alpha\right)$ was maintained over the entire angle-of-attack range except at angles of attack of about 25° and 75° where it dropped to about zero. At the higher angles of attack the pointed-nose model had generally better damping in roll than that of the rounded-nose model.

The data of figure 10(b) show that the damping in yaw for both configurations increased to very large values at an angle of attack of about 50° or 60° because of an increased damping contribution of the wing-fuselage combination. At angles of attack from about 25° or 30° to about 50° or 60°, the vertical tail was actually destabilizing.

SUMMARY OF RESULTS

The following results were obtained from an investigation of the low-subsonic static stability and damping derivatives at angles of attack from 0° to 90° for a model with a low-aspect-ratio unswept wing and two different fuselage forebodies:

1. Although the wing stalled at an angle of attack of about 12°, maximum lift did not occur until an angle of attack of about 40° or 50° was obtained. The static longitudinal stability of the model having a short rounded nose was greater than that of the model having a longer pointed nose over the entire angle-of-attack range. Some horizontal-tail effectiveness was maintained for both models beyond the angle of attack for maximum lift.

2. The pointed-nose model had large out-of-trim yawing moments above an angle of attack of about 40°. Shortening and rounding the nose of the model delayed these out-of-trim yawing moments to a slightly higher angle of attack.

3. Both models were directionally unstable above an angle of attack of about 20°, but both had positive effective dihedral over virtually the entire angle-of-attack range.

4. The rudder and aileron effectiveness decreased with increasing angle of attack, but some effectiveness was maintained over the angle-of-attack range shown.

5. At the higher angles of attack the pointed-nose model had generally better damping in roll than that of the rounded-nose model. Both models had very high damping in yaw at an angle of attack of about 50° or 60°.

Langley Research Center,
National Aeronautics and Space Administration,
Langley Field, Va., October 15, 1958.

REFERENCES

1. Hewes, Donald E.: Low-Speed Measurement of Static Stability and Damping Derivatives of a 60° Delta-Wing Model for Angles of Attack of 0° to 90°. NACA RM L54G22a, 1954.

2. Burk, Sanger M., Jr., and Hultz, Burton E.: Static Longitudinal Stability and Dynamic Characteristics at High Angles of Attack and at Low Reynolds Numbers of a Model of the X-3 Supersonic Research Airplane. NACA RM L50L19, 1951.

3. Letko, William: A Low-Speed Experimental Study of the Directional Characteristics of a Sharp-Nosed Fuselage Through a Large Angle-of-Attack Range at Zero Angle of Sideslip. NACA TN 2911, 1953.

TABLE I.- GEOMETRIC CHARACTERISTICS OF THE MODEL

Overall length of model having long pointed nose, ft	5.88
Overall length of model having shorter rounded nose, ft	4.75
Wing:	
Airfoil section	Modified hexagon
Span, ft	2.27
Area, sq ft	1.66
Aspect ratio	3.1
Thickness-chord ratio	4.5
Taper ratio	0.387
Root chord, ft	1.06
Tip chord, ft	0.41
Mean aerodynamic chord, $\bar{c}$, ft	0.78
Leading edge of mean aerodynamic chord rearward of leading-edge root chord, ft	0.21
Dihedral, deg	0
Incidence, deg	0
Sweepback of leading edge, deg	23
Ailerons:	
Area rearward of hinge line, sq ft	0.085
Span, percent of wing span	29.8
Horizontal tail:	
Airfoil section	Modified hexagon
Span, ft	0.98
Area, sq ft	0.31
Aspect ratio	3.1
Thickness-chord ratio	4.5
Taper ratio	0.40
Dihedral, deg	0
Incidence, deg	0
Sweepback of leading edge, deg	35
Vertical tail:	
Airfoil section	Modified hexagon
Span, ft	0.58
Total area, sq ft	0.237
Rudder area rearward of hinge line, sq ft	0.61
Aspect ratio	1.4
Thickness-chord ratio	4.5
Taper ratio	0.298
Sweepback of leading edge, deg	45

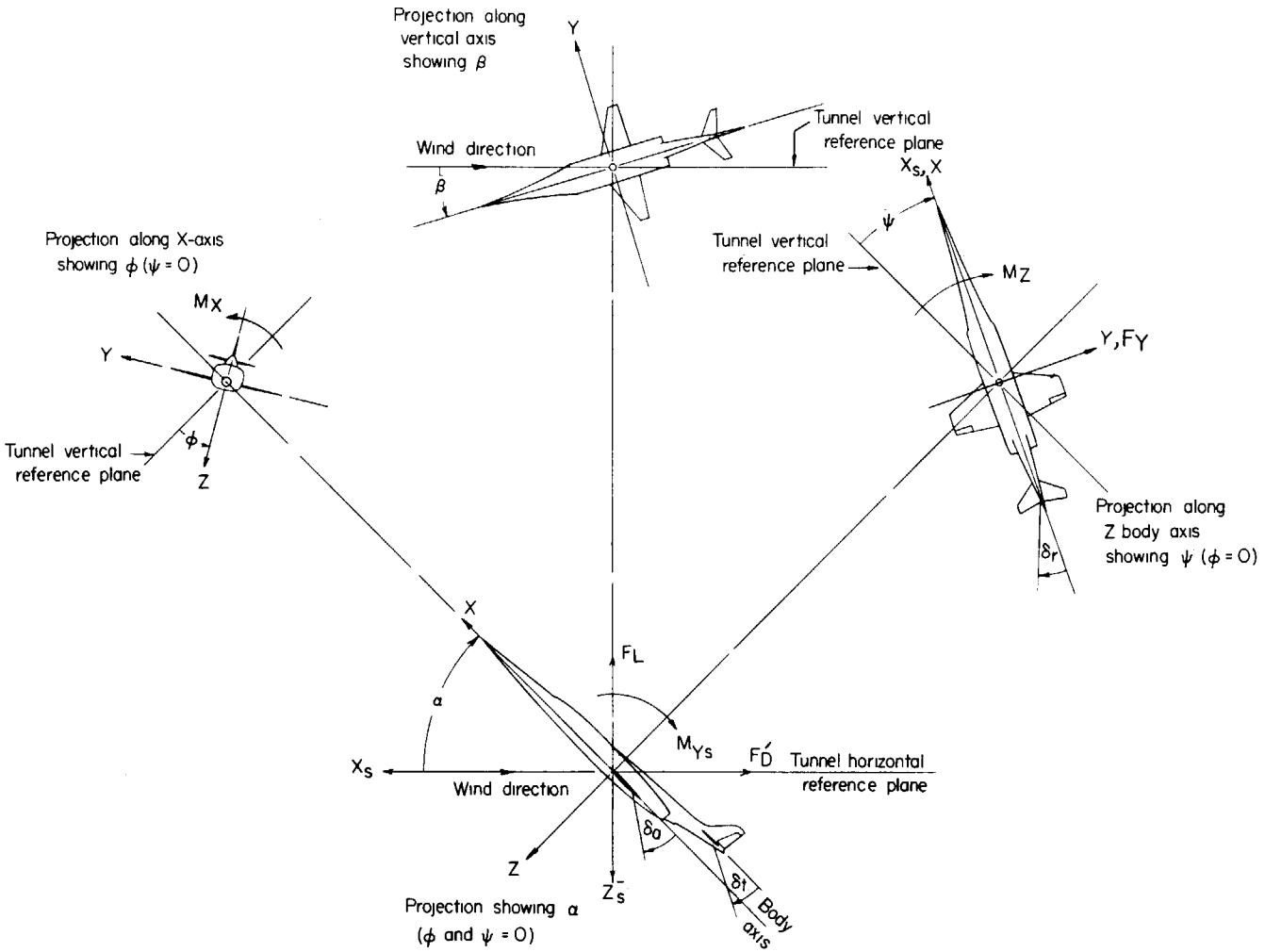

Figure 1.- System of axes used in the investigation. Longitudinal-stability data are referred to the stability system of axes, and the lateral-stability data are referred to the body system of axes. Arrows indicate positive directions of moments, forces, and angles.

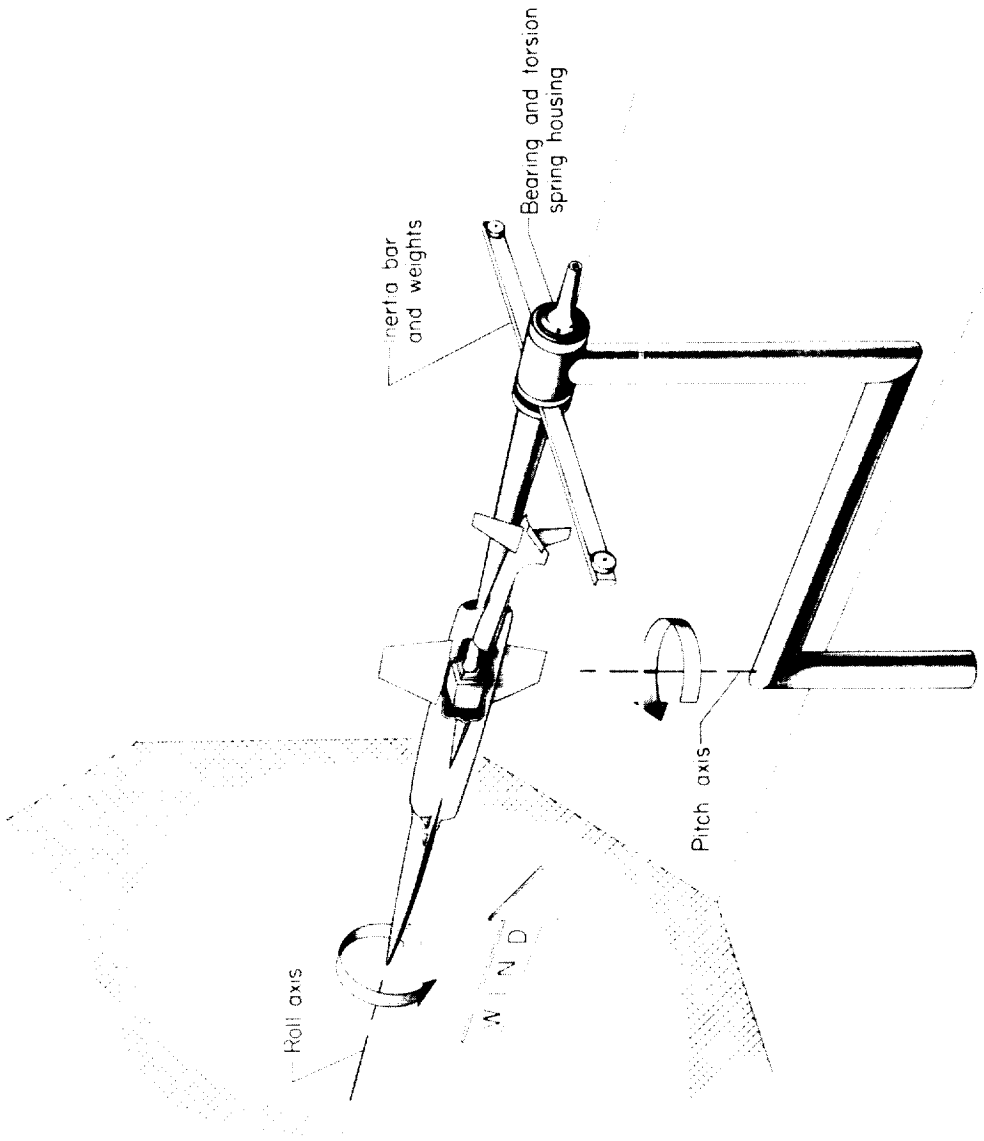

(a) Model mounted for damping-in-roll tests.

Figure 2.- Sketch of dynamic-test setup.

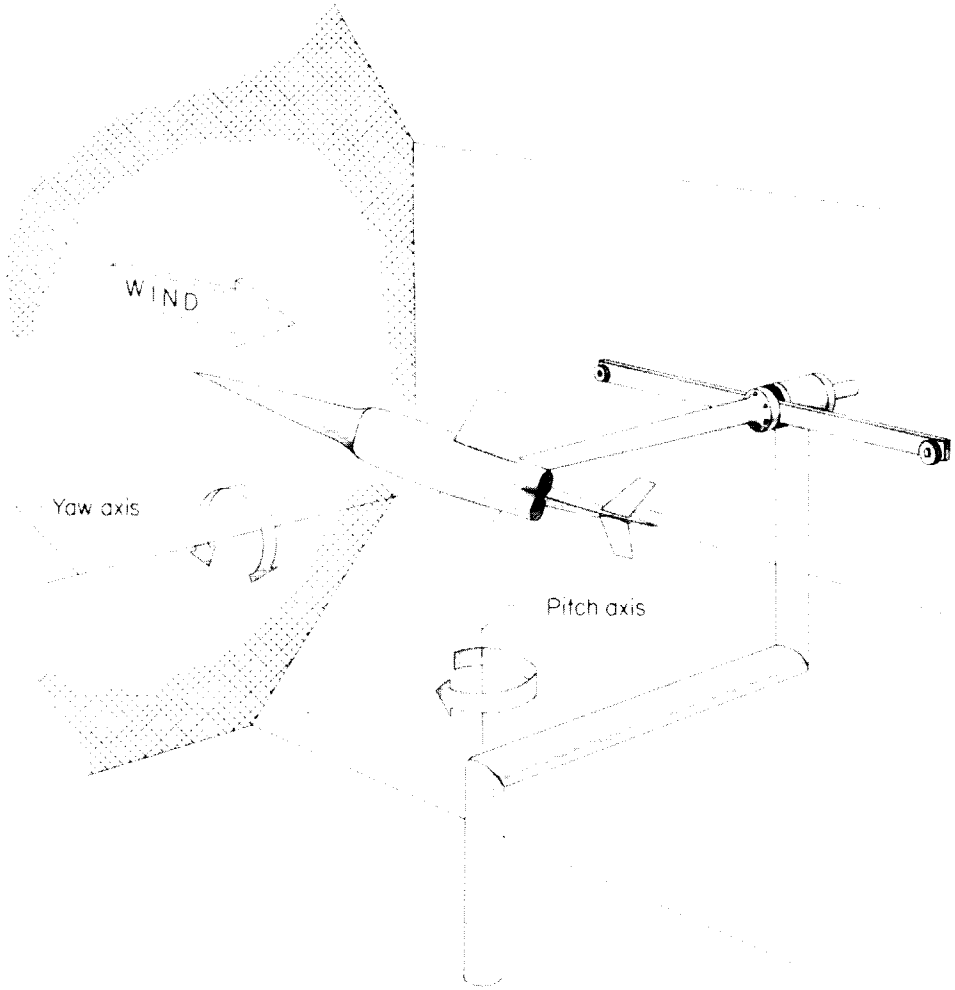

(b) Model mounted for damping-in-yaw tests.

Figure 2.- Concluded.

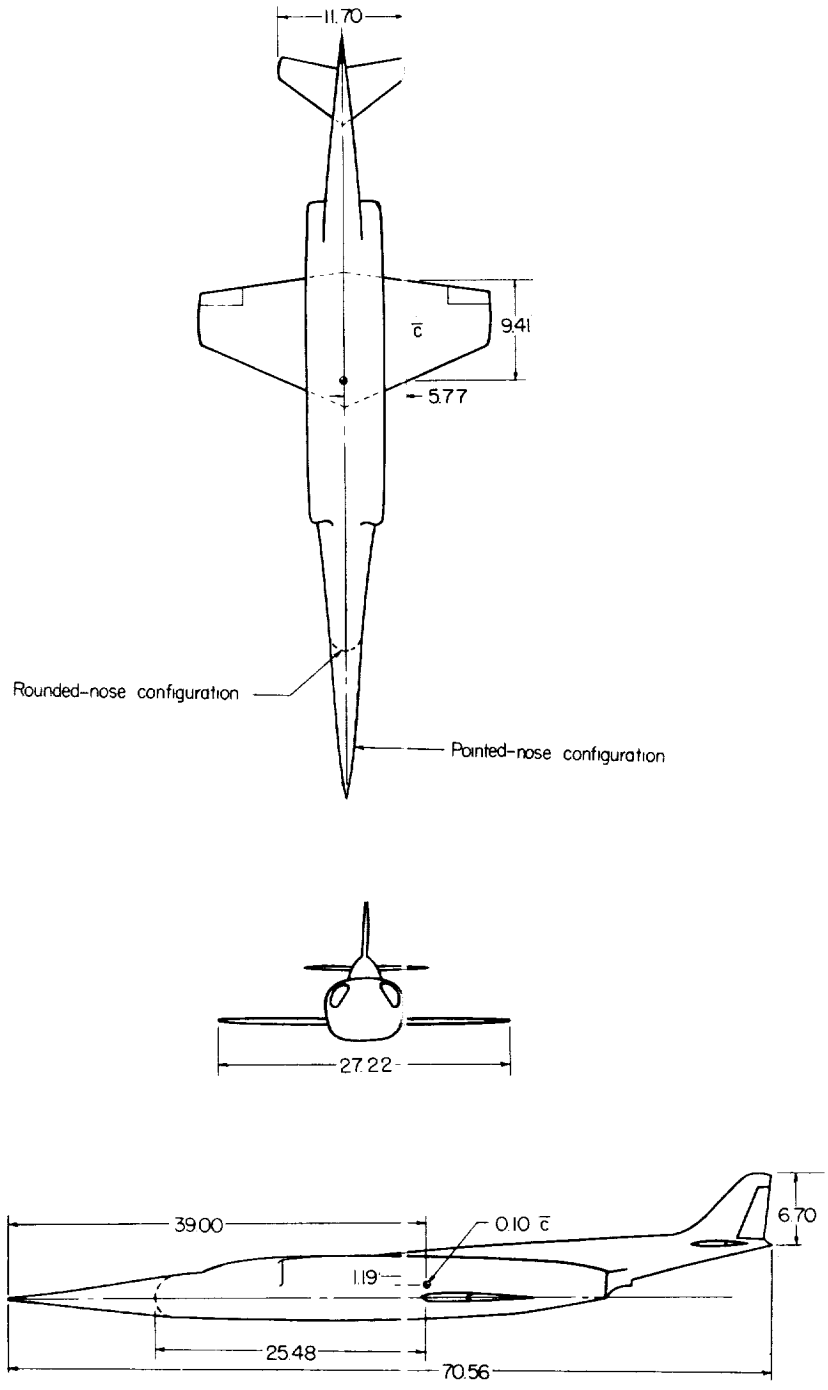

Figure 3.- Three-view drawing of model used in investigation. All dimensions are in inches.

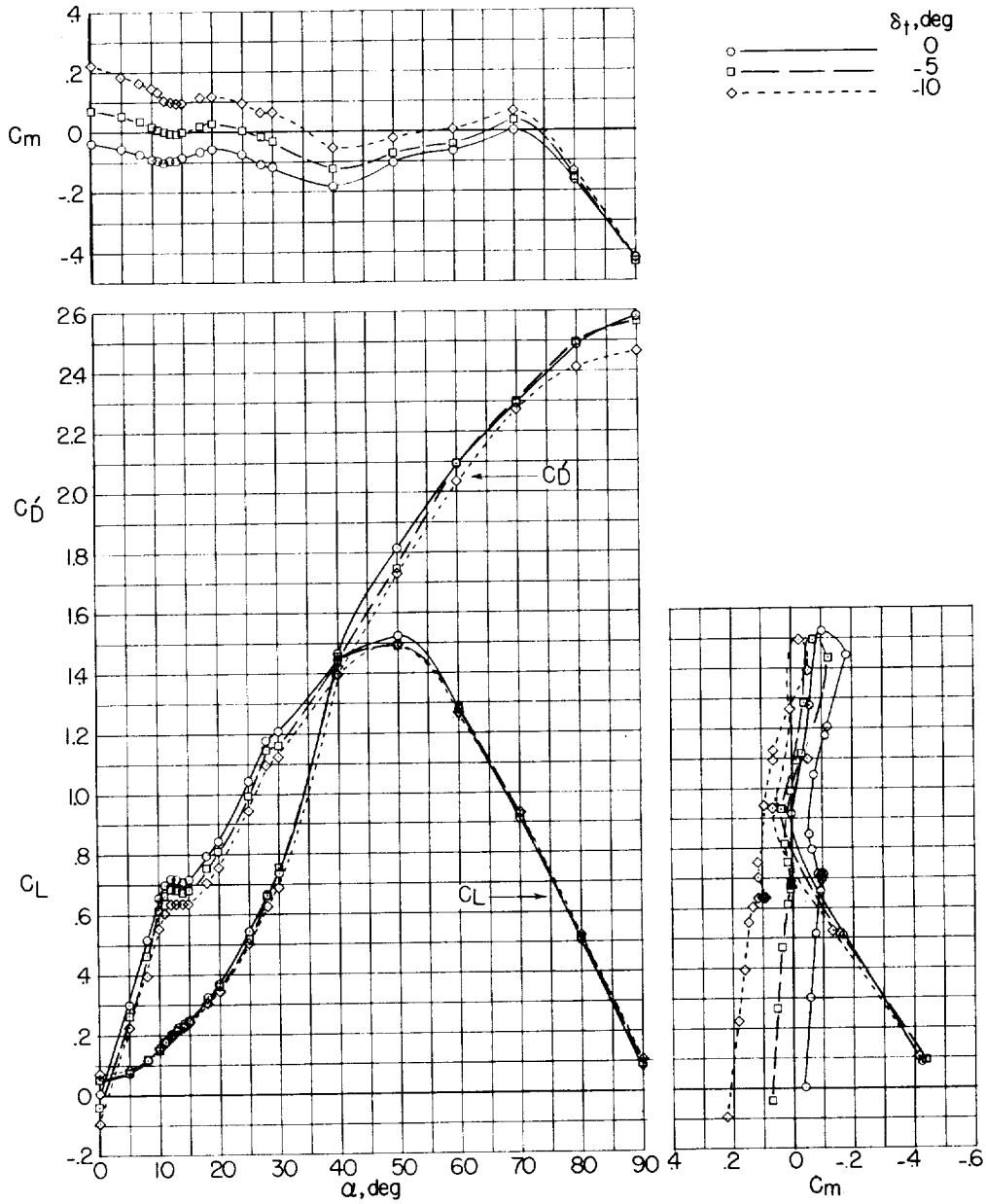

(a) Pointed-nose model.

Figure 4.- Static-force-test data showing variation of pitching-moment, drag, and lift coefficients with angle of attack.

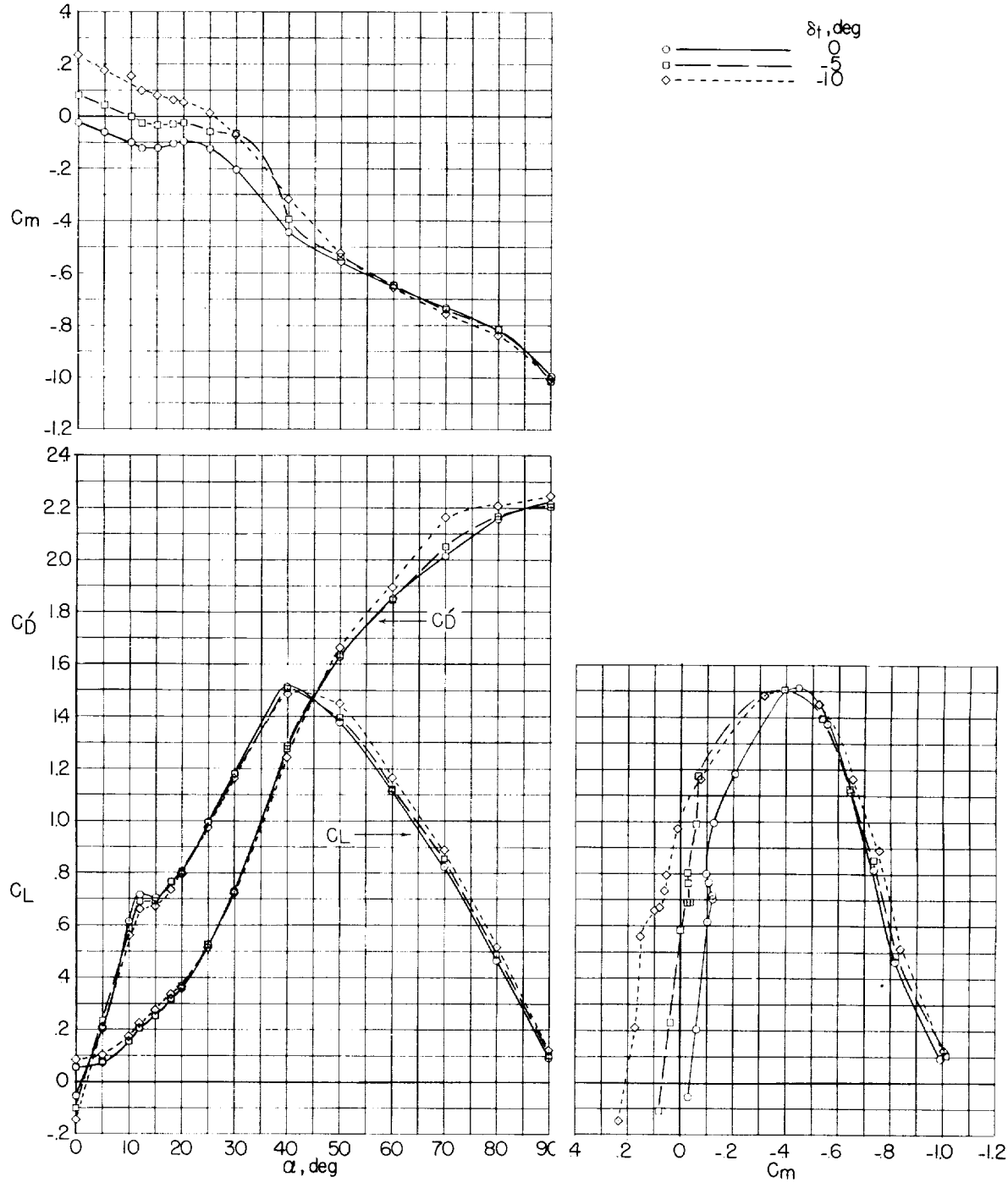

(b) Rounded-nose model.

Figure 4.- Concluded.

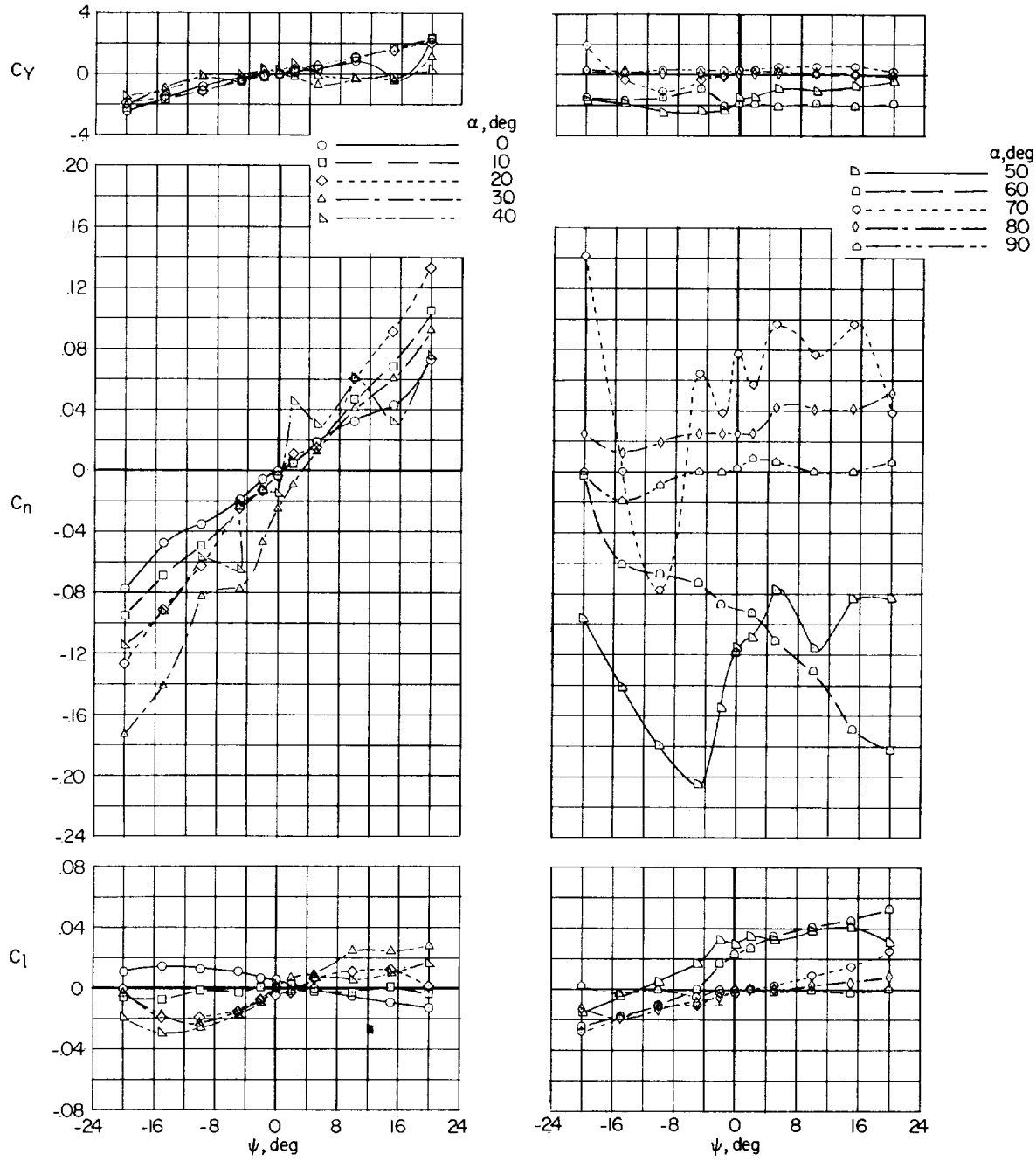

(a) Vertical and horizontal tails off.

Figure 5.- Static-force-test data showing variation of lateral-force, yawing-moment, and rolling-moment coefficients with angle of yaw for model having a long pointed nose at various angles of attack. $\phi = 0^\circ$.

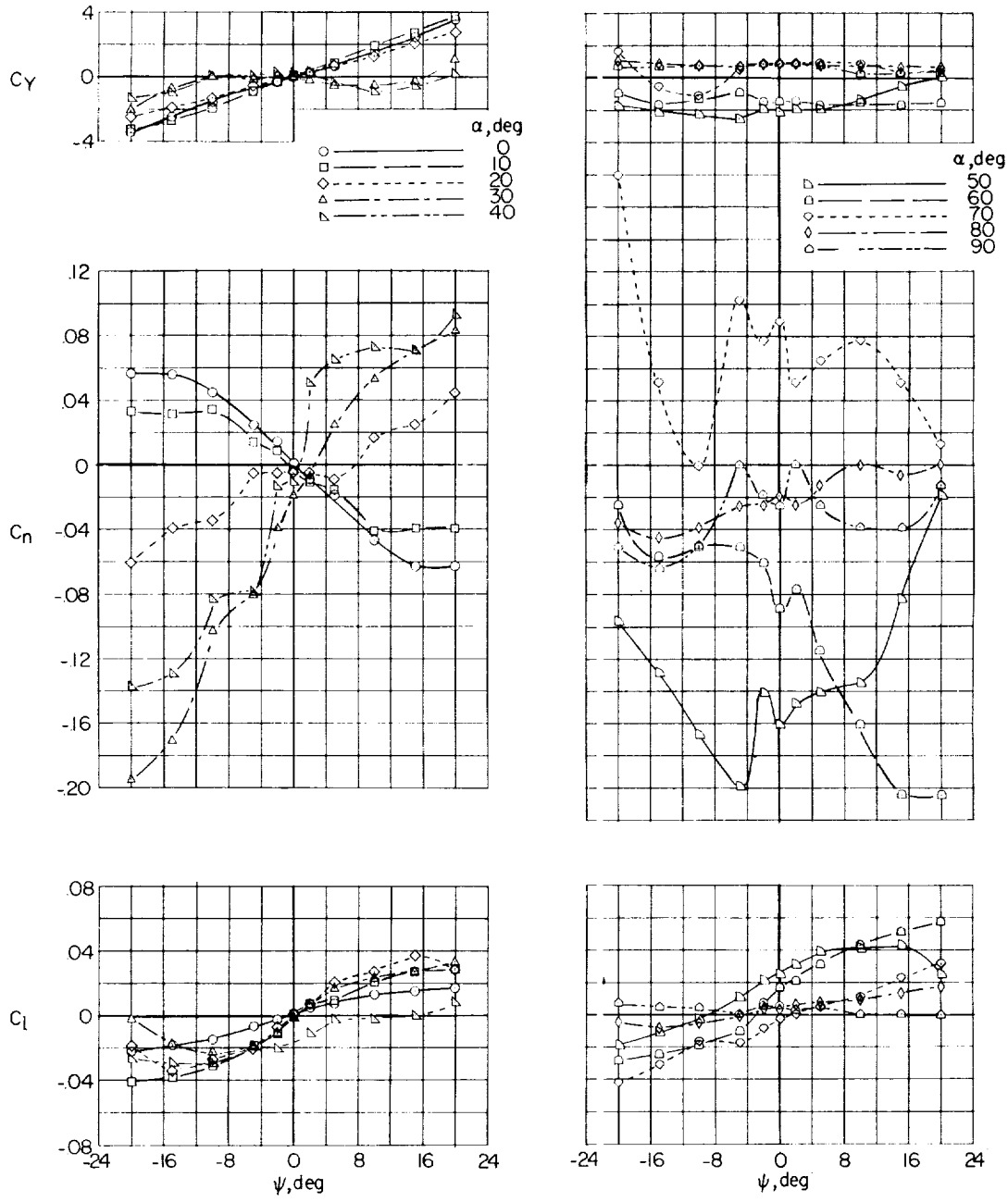

(b) All tails on. $\delta_t = 0^o$.

Figure 5.- Concluded.

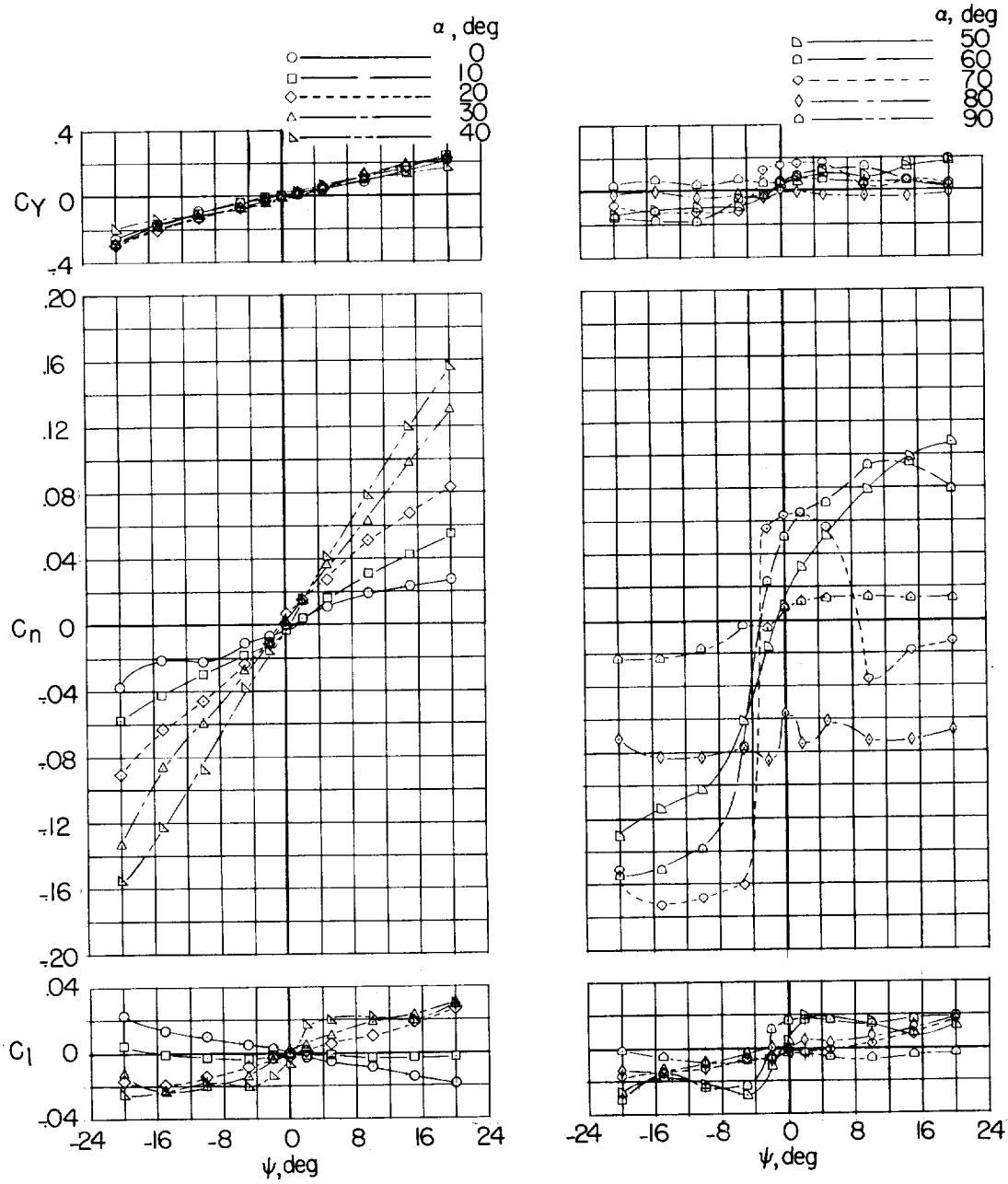

(a) Vertical and horizontal tails off.

Figure 6.- Static-force-test data showing variation of lateral-force, yawing-moment, and rolling-moment coefficients with angle of yaw for model having a shorter rounded nose at various angles of attack. $\phi = 0^{\circ}$.

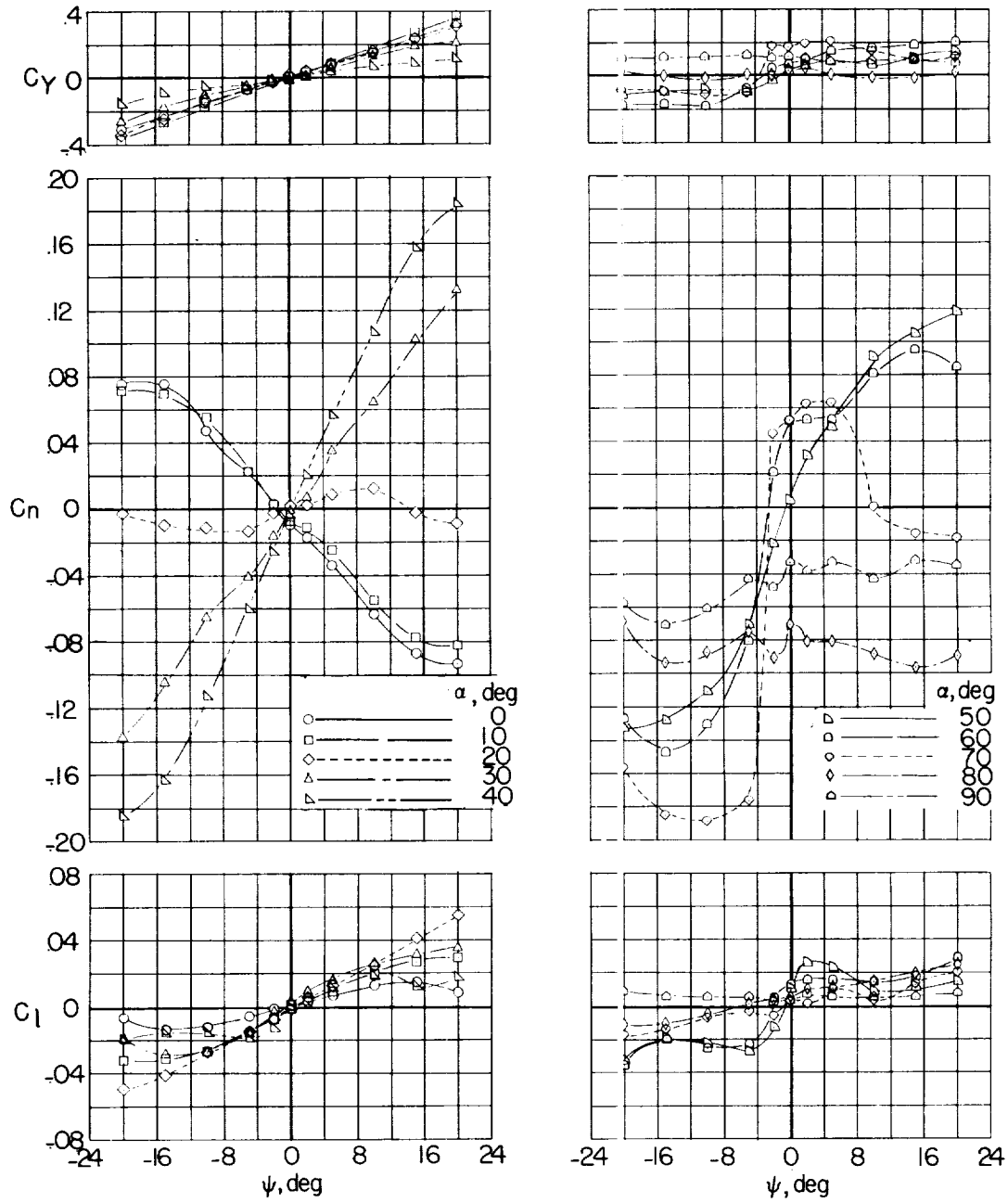

(b) All tails on. $\delta_t = 0^\circ$.

Figure 6.- Concluded.

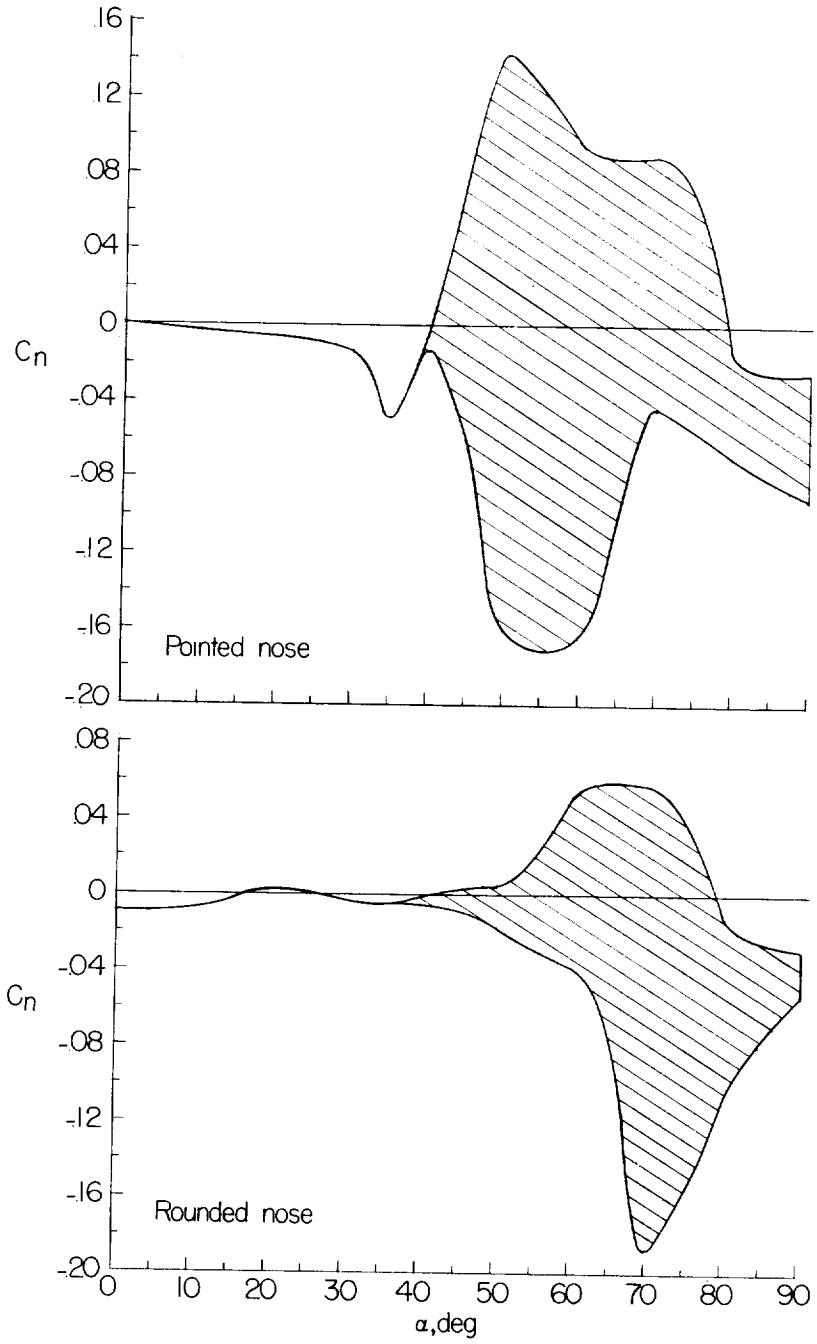

Figure 7.- Variation of yawing-moment coefficient with angle of attack for models with all tails on. Shaded area shows range of readings obtained in several check tests made at the higher angles of attack. $\psi = 0^{\circ}$; $\delta_t = 0^{\circ}$.

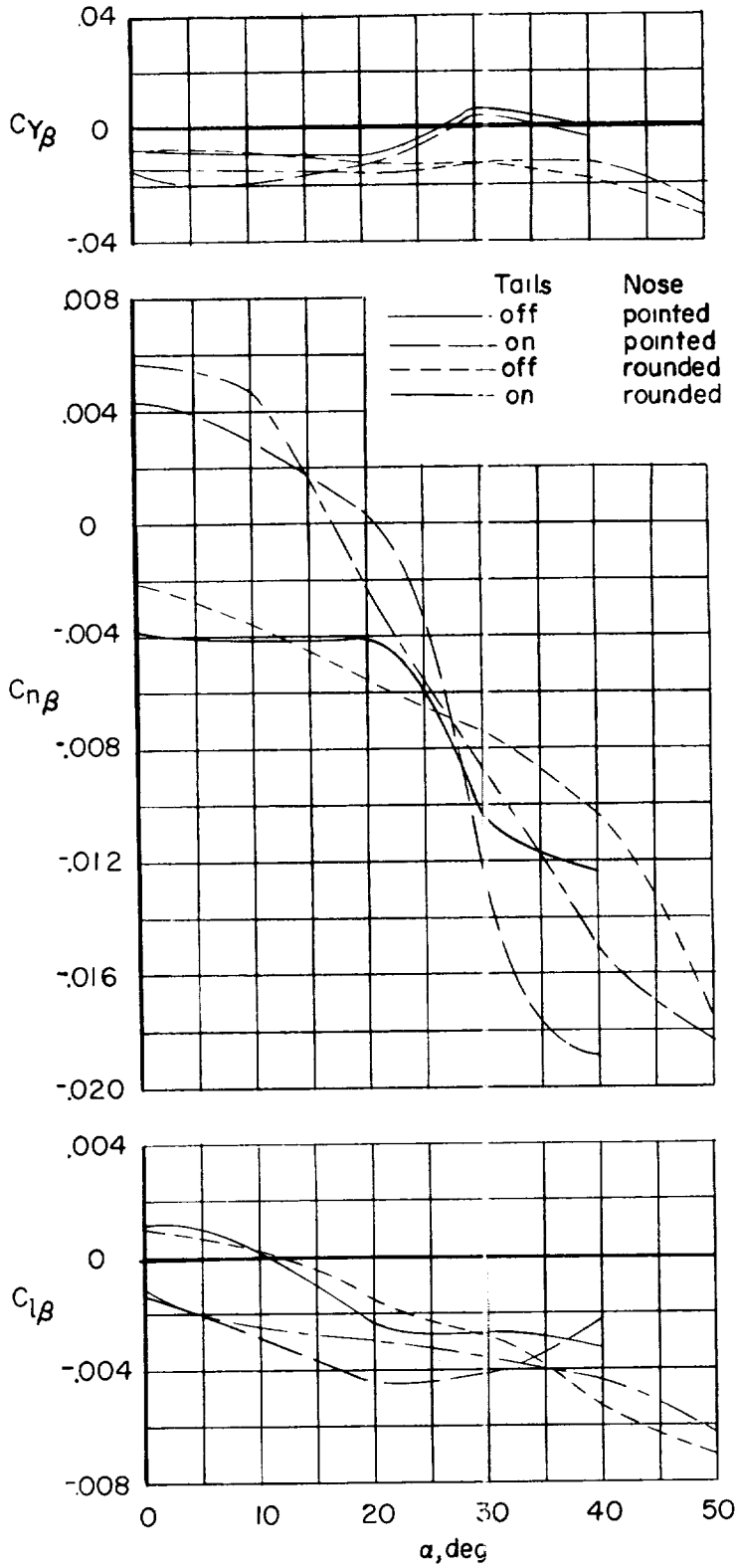

Figure 8.- Variation of sideslip derivatives with angle of attack.

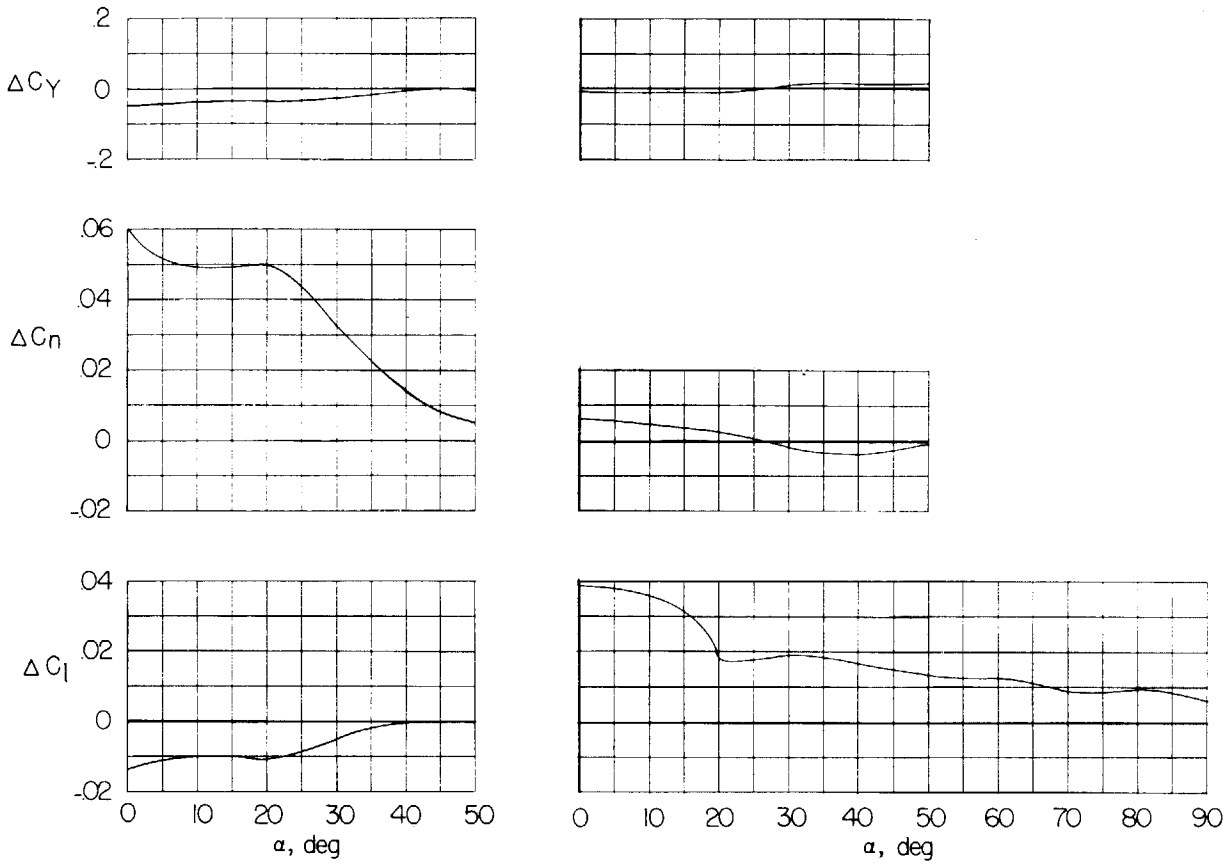

(a) Rudder effectiveness. Rudder deflected -20°.

(b) Aileron effectiveness. Ailerons deflected a total of 40° ($\delta_{a,L} = 20°$ and $\delta_{a,R} = -20°$).

Figure 9.- Increments in lateral-force, yawing-moment, and rolling-moment coefficients (ΔC_Y, ΔC_n, and ΔC_l, respectively) plotted against angle of attack for deflection of rudder and ailerons for the rounded-nose model.

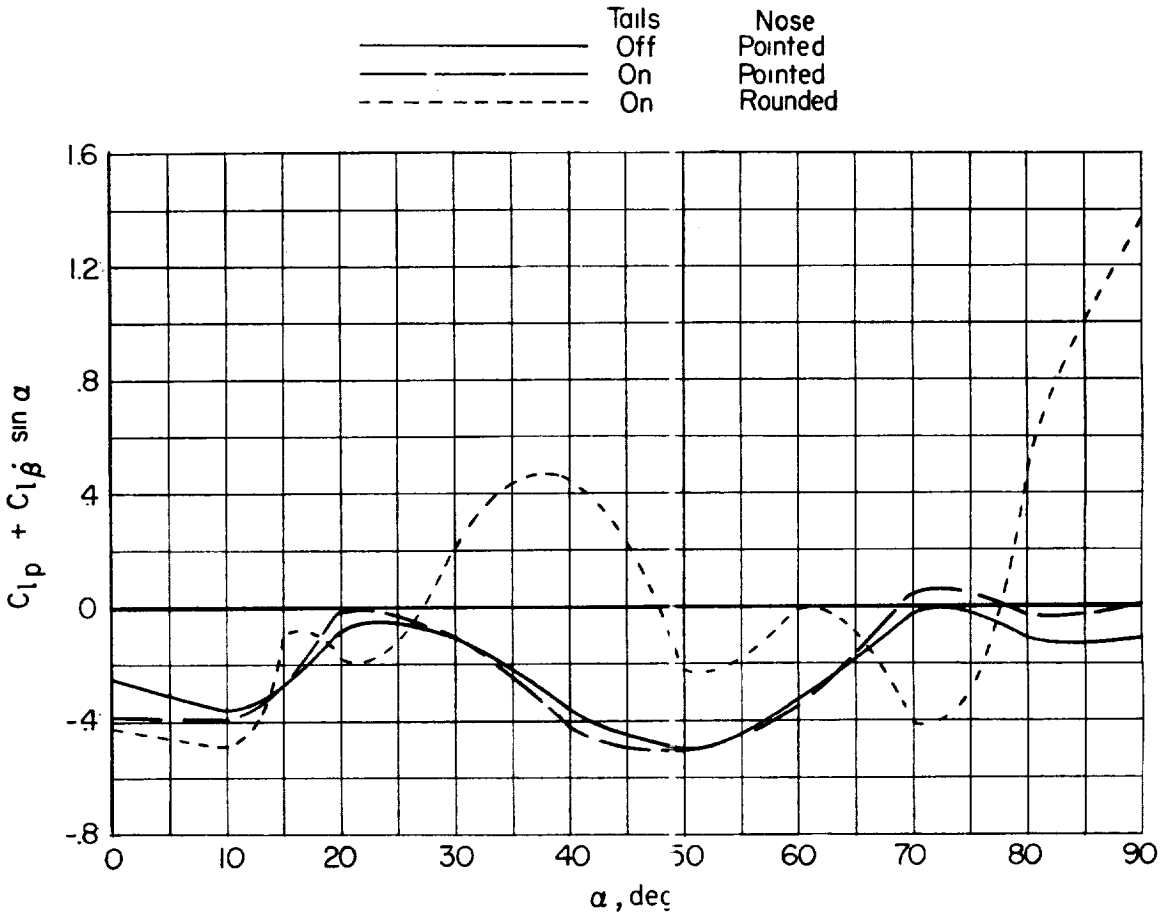

(a) Damping in roll.

Figure 10.- Variation of damping-in-roll and damping-in-yaw derivatives with angle of attack.

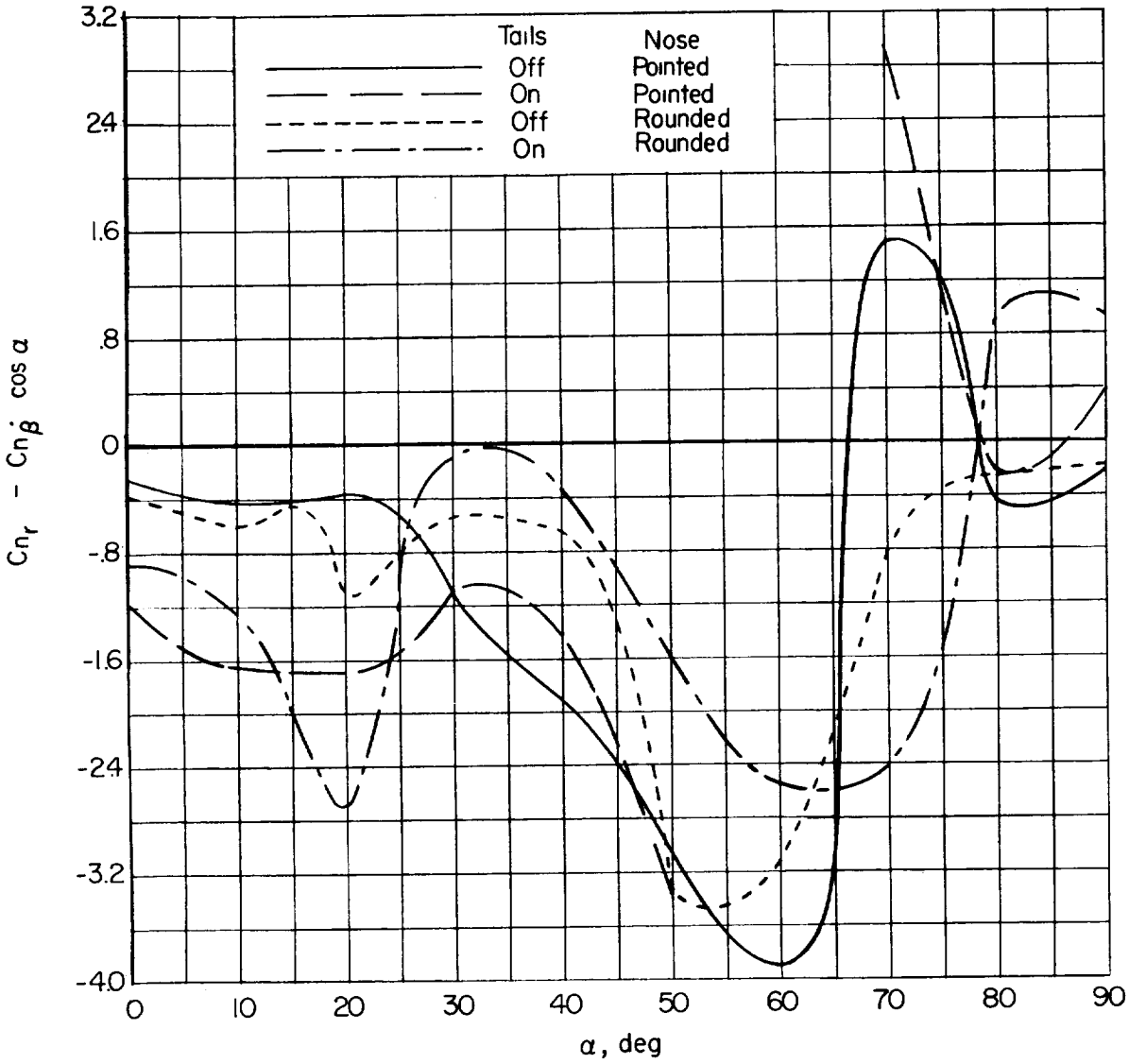

(b) Damping in yaw.

Figure 10.- Concluded.

NASA - Langley Field, Va. L-151